

Detection prospects of Very and Ultra High-Energy gamma rays from extended sources with ASTRI, CTA, and LHAASO

S. Celli^{1,2,3} and G. Peron^{4,5}

¹ Sapienza Università di Roma, Physics Department, P.le Aldo Moro 2, 00185, Rome, Italy

² Istituto Nazionale di Fisica Nucleare, Sezione di Roma, P.le Aldo Moro 2, 00185, Rome, Italy

³ Istituto Nazionale di Astrofisica, Osservatorio Astronomico di Roma, Monte Porzio Catone, Rome, Italy

⁴ Istituto Nazionale di Astrofisica, Osservatorio Astrofisico di Arcetri, L.go E. Fermi 5, Firenze, Italy

⁵ Université Paris Cité, CNRS, Astroparticule et Cosmologie, F-75013 Paris, France

e-mail: silvia.celli@uniroma1.it, giada.peron@inaf.it

March 7, 2024

ABSTRACT

Context. The recent discovery of several ultra high-energy gamma-ray emitters in our Galaxy constitutes a significant advancement towards unveiling its most powerful accelerators and their properties. Nonetheless, in order to unambiguously locate the regions where the highest energy particles are produced and understand the responsible physical mechanisms, detailed spectral and morphological studies are required, especially given that most of the observed sources were found to be significantly extended.

Aims. In these regards, pointing observations with the next-generation Imaging Atmospheric Cherenkov Telescopes, like the Cherenkov Telescope Array (CTA) Observatory and the ASTRI Mini-Array (ASTRI), are expected to provide significant improvements. Here we aim at identifying the most promising sources to target in future observations.

Methods. To this purpose, we performed a comparative analysis of the expected performance of ASTRI and CTA, computing their differential sensitivities towards extended sources, and further explored their capabilities with respect to specific case studies, including follow-ups of existing gamma-ray source catalogs.

Results. We find that almost all of the sources so far detected by LHAASO-WCDA and HGPS will be in the reach of ASTRI and CTA with 300 and 50 hours of exposure, respectively. For the highest energy emitters detected by LHAASO-KM2A, in turn, we provide the list of the most promising objects to be investigated. We further examined specific classes of sources in order to identify potentially detectable gamma-ray emitters, such as passive molecular clouds (i.e. illuminated by the cosmic-ray sea) and pulsars surrounded by a halo of runaway particles.

Key words. Radiation mechanisms: non-thermal – Catalogs – ISM: cosmic rays – ISM: clouds – Telescopes – Astroparticle physics

1. Introduction

In recent years, gamma-ray astronomy has witnessed a significant experimental boost. In the context of the so-called Extensive Atmospheric Shower (EAS) ground-based detectors, the Large High Altitude Air Shower Observatory (LHAASO) started operating in its full configuration in 2021, opening a new observational window into the electromagnetic sky above 100 TeV. Thanks to its large effective area and efficient background rejection, LHAASO achieved in the first year of data acquisition an unprecedented sensitivity, enabling the discovery of few tens of Ultra High-Energy (UHE, i.e. $E \gtrsim 100$ TeV) emitters (Cao et al. 2023). The identification of these source is still uncertain, partly due to the limited angular resolution of its detection technique. In fact, most of the observed sources have a large angular extension and are located in crowded regions of the Galactic Plane, thus increasing the chances for source confusion.

Meanwhile, significant improvements are foreseen regarding Imaging Atmospheric Cherenkov Telescopes (IACTs), with the ongoing construction of the ASTRI Mini-Array (*Astrofisica con Specchi a Tecnologia Replicante Italiana*, hereafter ASTRI) and the Cherenkov Telescope Array Observatory (CTAO, hereafter CTA). ASTRI is a nine-telescopes array (one telescope is already operative) currently under construction in Tenerife (Spain) (Vercellone et al. 2022a). In its final configuration, which is expected

to be completed in the next few years, ASTRI will be sensitive to energies up to 200 TeV with an improved sensitivity compared to the currently operating IACTs (MAGIC, VERITAS and H.E.S.S.) above a few TeV (Lombardi et al. 2022). CTA will in turn consist of two arrays, one located in La Palma (Spain) and the other in Paranal (Chile), thus covering both the Northern and the Southern hemisphere. Once completed, CTA will reach a sensitivity one order of magnitude lower than the currently-operating IACTs, spanning a broad energy interval ranging from a few tens of GeV to a few hundreds of TeV (Cherenkov Telescope Array Consortium et al. 2019).

The advantage of detecting photons with arrays of IACTs is above all their superior angular resolution ($\lesssim 3$ arcmin), peculiar of the stereoscopic technique (Aharonian et al. 2013). This is a key feature for obtaining a clear source identification and to conduct precise morphological investigations, capable of distinguishing the sites of particle acceleration from nearby regions (e.g. molecular clouds illuminated by escaped particles). Furthermore, the larger Field of View (FoV) of the next-generation IACTs (up to $\sim 10^\circ$ in diameter) will allow us to study and resolve large and crowded sources such as supernova remnants, pulsar wind halos, and superbubbles.

Nevertheless, observations suffer from a degraded performance with respect to the ideal on-axis point-like case, due to both

off-axis pointing and increased background in extended analyses, which also affects the minimum source flux detectable by IACTs. As shown in Ambrogi et al. (2018) for a previous CTA layout (the so-called 2Q-array), the extent of the worsening depends on the energy range of the observations, and it tends to disappear at the highest energies. Thus, a more accurate evaluation of the detection prospects and required exposure per source is necessary when dealing with extended sources. We here update those predictions by considering the most up-to-date CTA proposed layout, the so-called Alpha configuration¹. In addition, we compute the expected ASTRI and LHAASO sensitivities towards extended sources. Such investigations allow us to clearly define a sample of gamma-ray sources that will be detectable by the next-generation IACTs, which is crucial to outline an optimized observational plan. We start by summarizing the detection techniques of these instruments in Sec. 2, and later describe their specific features in Sec. 3. We then introduce the methods that we developed for computing the instrument sensitivities for extended source observations in Sec. 4, and discuss the obtained results. As an application of the derived minimum detectable fluxes, in Sec. 5 we present cases demanding for tailored IACT observations aimed at obtaining improved morphological and spectral information. Particularly, in Sec. 5.1 we scan existing gamma-ray source catalogs in the Very High-Energy (VHE, i.e. $E \gtrsim 100$ GeV) and UHE bands to define promising candidates for observations, while in the following subsections we discuss perspectives for detecting PeVatrons, passive molecular clouds illuminated by cosmic rays, and TeV halos. We finally draw our conclusions in Sec. 6. Three appendices complement the text: in Appendix A we discuss IACT response functions to off-axis sources, in Appendix B we present IACT differential sensitivities in high-zenith angle observations, and finally in Appendix C we provide a comparison among our results and official point-like source sensitivities from ASTRI, CTA, and LHAASO, also exploring individual sub-array configurations of CTA.

2. Detection methods of VHE gamma rays

The Earth atmosphere is opaque to gamma rays, consequently ground-based detection methods rely on the indirect measurements of the secondary particles that compose the cascades generated by photons. Two main detection techniques exist for measuring such emission: the IACT technique, based on the observation of the Cherenkov flashes induced by the superluminal shower particles traversing the atmosphere; and the EAS technique, aimed at collecting individual shower particles from ground. The discrimination of photon- from hadron-induced showers is a fundamental part of the measurements. In the following we describe the different detection and background rejection methods implemented by the present and next-generation instruments.

2.1. IACTs: CTA and ASTRI

Large ($\gtrsim 1$ m²) optical reflectors, combined with fast (~nanoseconds) cameras sensitive to blue (300-350 nm) light, permit the detection of the Cherenkov emission of the shower ultra-relativistic secondary particles. Because of the signal faintness, IACTs operate only at night, when the Moon contribution is limited, and in good weather conditions, reducing the duty cycle of these detectors ranging in 10-20%. The

stereoscopic distribution of the collectors in arrays of multiple telescopes enables a better determination of the arrival direction of the shower, guaranteeing angular resolution of the order of a few arcminutes (Aharonian et al. 2013). Hadron-initiated showers are also detected by IACTs: as they constitute a background for photon-induced cascades, hadronic showers need to be rejected after the data acquisition (Maier & Knapp 2007). A first gamma/hadron separation is conducted based on the projected shape of the Cherenkov-light cone on the camera (Hillas 1985): the high transverse momentum of secondary hadrons, in fact, induces a highly scattered distribution of hadronic showers at fixed energy of the primary. Nonetheless, an irreducible background of gamma-ray like hadron will survive the separation cuts. Such a residual hadronic emission is estimated at the level of the analysis, e.g. by evaluating the background in a source-free region or by fitting a background template to the data in the region of interest (Berge et al. 2007). The two methods have been extensively tested for H.E.S.S. data analysis showing equivalent results.

The future of IACTs foresees two new facilities. ASTRI at its completion will be an array of nine telescopes located at the *Observatorio del Teide* in Tenerife (28°17'60.00"N, 16°30'20.99"W) at an altitude of approximately 2370 m. Each of the telescopes will have two mirrors in the Schwarzschild-Couder design, of 4.3 m and 1.8 m diameter respectively, whose size allows the array to best perform in the energy range around 10 TeV. The telescopes are equipped with a wide FoV camera, about 10° in diameter, constituted by silicon photo multipliers (Scuderi et al. 2022; Catalano et al. 2018).

CTA will be an observatory located at two sites: the Northern hemisphere array, so-called CTA-North, designated area is in the Canary Island of La Palma (28°45'43.7904"N, 17°53'31.218"W), while the Southern array, so-called CTA-South, in the Paranal plateau in Chile (4°41'0.34"S, 70°18'58.84"W). The final CTA layout (the *Alpha* configuration) has been recently established: it consists of 4 Large-Size Telescopes (LSTs, one of which is already operating) and 9 Medium-Size Telescope (MSTs) for the Northern array, versus 14 MSTs and 37 Small-Size Telescopes (SSTs) for the Southern site. The diameters of the main reflecting surface of the telescopes will be of 23, 11.5, and 4.3 m respectively for the large, medium and small size type, while their FoV will be $> 4.5^\circ$, $> 7^\circ$, and $> 8^\circ$ respectively (Cherenkov Telescope Array Consortium et al. 2019). The use of many SSTs, distributed on a large (~3 km²) area is expected to improve the detection at high (5-300 TeV) energies, while the employment of the LSTs will allow reaching a better sensitivity at lower (20–150 GeV) energies. Further improvements with respect to the Alpha configuration are expected as a result of the CTA+ program², that has been recently approved and funded for the procurement of two more LSTs and five SSTs specifically for the CTA-South site (Antonelli 2023).

2.2. EAS arrays: LHAASO

LHAASO is an EAS observatory built at 4400 m above sea level in the Sichuan province of China. It consists of three type of detectors designed for the study of Cosmic Rays (CRs) and gamma rays across a broad energy range from sub-TeV to beyond the PeV energy scale: the Water Cherenkov Detector Array (WCDA), the Square Kilometer Array (also called KM2A), and

¹ <https://www.cta-observatory.org/science/ctao-performance/>

² <https://pnrr.inaf.it/progetto-ctaplus/>

the Wide Field-of-view Cherenkov Telescope Array (WFCTA). The WCDA is a 78000 m² surface water Cherenkov pond, filled with purified water and equipped with upward facing photomultiplier tubes (PMTs). The KM2A is an array composed of 5195 Electromagnetic Detectors (EDs) and 1188 Muon Detectors (MDs), extending for 1.3 km² surface. EDs are plastic scintillators detecting the electromagnetic component of EASs, covered by a lead plate (0.5 cm thick) and a 1.5" PMT. MDs are in turn cylindric muon tanks, filled with pure water and buried under 2.5 m of soil, as to absorb the electromagnetic component and detect the muonic component of an EAS. The two instruments operate independently, with a core energy range of ~ 100 GeV to ~ 50 TeV for WCDA, and between ~ 10 TeV and ~ 10 PeVs for KM2A. Finally, 12 wide field of view air Cherenkov telescopes compose the WFCTA, complementing the system in CR observations; given that these are not used in gamma-ray related studies, we will not discuss WFCTA further. The LHAASO operation principle relies on combining information about the collected PMT hit and charge distributions to evaluate shower parameters, as its core location (i.e. the expected position on ground of the primary particle), size (i.e. number of secondary particles), age (related to the amount of traversed matter in the atmosphere) and muon content. From this information, the primary's arrival direction, energy and nature (hadronic vs electromagnetic) can be determined. Indeed, in the case where the primary is a CR entering the Earth's atmosphere, the air shower consists of secondary hadrons, muons, leptons, and photons, while in the case of primary photons the cascade is purely electromagnetic, consisting of leptons and photons. In KM2A, the ratio among the measured number of electrons and muons is used to separate CR from gamma-ray induced showers. In WCDA, additional parameters are used for CR rejection, e.g. the shower compactness, which is determined by the measurement of the effective charge beyond a given position from the shower axis (expected to be larger for CR-induced showers).

The observatory was completed in mid 2021: its high sensitivity, particularly at the highest energies probed by KM2A and so far unexplored, was essential to detect the emission of PeV photons from several Galactic accelerators (Cao et al. 2021).

3. Instrument response functions

A proper comparison among instruments relying on different detection techniques and operating in different energy ranges is only possible through the evaluation of differential sensitivities, establishing the minimum detectable flux in each energy bin. Their computation, presented in the following section, is based on certain parameters, namely the same energy binning, observation time and detection thresholds, as well as on individual Instrument Response Functions (IRFs), specifically angular and energy resolutions, effective area, and expected background rate. We here proceed to the description of the latter quantities, according to the latest available official releases by each Collaboration.

3.1. LHAASO IRFs

We adopt the most recent response functions for LHAASO-KM2A, calibrated in the analysis of the Crab Nebula (Dong et al. 2024). We make use specifically of the IRFs relative to observations at zenith angle $\theta = 20^\circ$, to be consistent with those released by ASTRI. Updated responses of the WCDA detector are not yet available, thus we here limit our investigations to

KM2A. We consider the response functions as angular resolution, effective area to gamma rays, and gamma/hadron separation efficiency, all provided at analysis level, i.e. including both cuts for hadron rejection as well as quality cuts selecting well reconstructed events. The IRFs released so far use event selection cuts optimised for point sources as the optimisation for extended sources requires additional care. We expect analyses of extended sources to require more stringent cuts to reduce the background rate, which impacts the effective area. Hence, they require a dedicated investigation by the collaboration itself, that may be available in the next future.

While gamma-ray effective area, angular/energy resolution are provided in the IRFs, the expected background rate can be derived by convolving the all-particle CR flux (taken from Gaisser et al. (2013)) with the effective area to hadronic showers at analysis level. The latter is obtained directly from the available photon effective area, which is first divided by the gamma-ray selection efficiency, and then multiplied for the CR rejection power as provided in Dong et al. (2024). We finally integrate the resulting area with the all-particle CR flux and derive the quantity shown as a yellow line in Fig. 1c. It is worth noticing that LHAASO-KM2A obtains its high rejection power thanks to the usage of muons for hadron identification: this is particularly important at the highest energies, where the increased abundance of muons facilitates the identification of the nature of primary particles.

3.2. CTA and ASTRI IRFs

Fig. 1 also shows the IACT IRFs for on-axis observations (while IRFs for off-axis observations at different offsets from the FoV center are shown in Appendix A) for both ASTRI and the two CTA observatories. The latter can be retrieved in publicly available zenodo repositories (ASTRI-Project 2022; Cherenkov Telescope Array Observatory & Cherenkov Telescope Array Consortium 2021). Nominal pointing is assumed in the simulations, with all telescopes pointing to the same direction; different configurations are currently under investigation by the Collaborations.

A direct comparison among LHAASO, ASTRI, and CTA IRFs is now possible given that the same energy binning was set, namely 0.2 in logarithmic scale. The excellent angular resolution of IACTs, due to their pointing technique and camera, is visibly superior to the one of LHAASO-KM2A: in fact, the 1σ width of Point Spread Function (PSF) amounts to $\sigma_{\text{PSF}} \lesssim 0.1^\circ$ for IACTs vs $\sigma_{\text{PSF}} \gtrsim 0.1^\circ$ for LHAASO. With regards to the effective area, instead, for EAS arrays, it coincides with the geometrical area, namely the instrument surface exposed to the shower, since shower reconstruction relies on the number of particles collected on ground. In the case of LHAASO, a surface of 1 km² is covered by the KM2A. On the other hand, the effective area of IACTs is rather a convolution between the geometrical area and the Cherenkov light pool illuminated by the gamma-ray induced shower. The former depends on the specific layout of the experiment, namely by the relative distance among telescopes. For ASTRI, the foreseen layout covers an area of about 600×300 m² (Vercellone et al. 2022a), while CTA-North of about 600×450 m² and CTA-South of about 2000×1800 m² (Cherenkov Telescope Array Consortium et al. 2019). On the other hand, the Cherenkov pool of a primary photon interacting at a height of about 10 km spreads over a surface on ground of 3×10^4 m² (Aharonian et al. 2013); this value hence represents the effective area of an individual imaging telescope, which has to be rescaled to the number of telescopes when providing a description of the array. The effective areas shown in Fig. 1 are

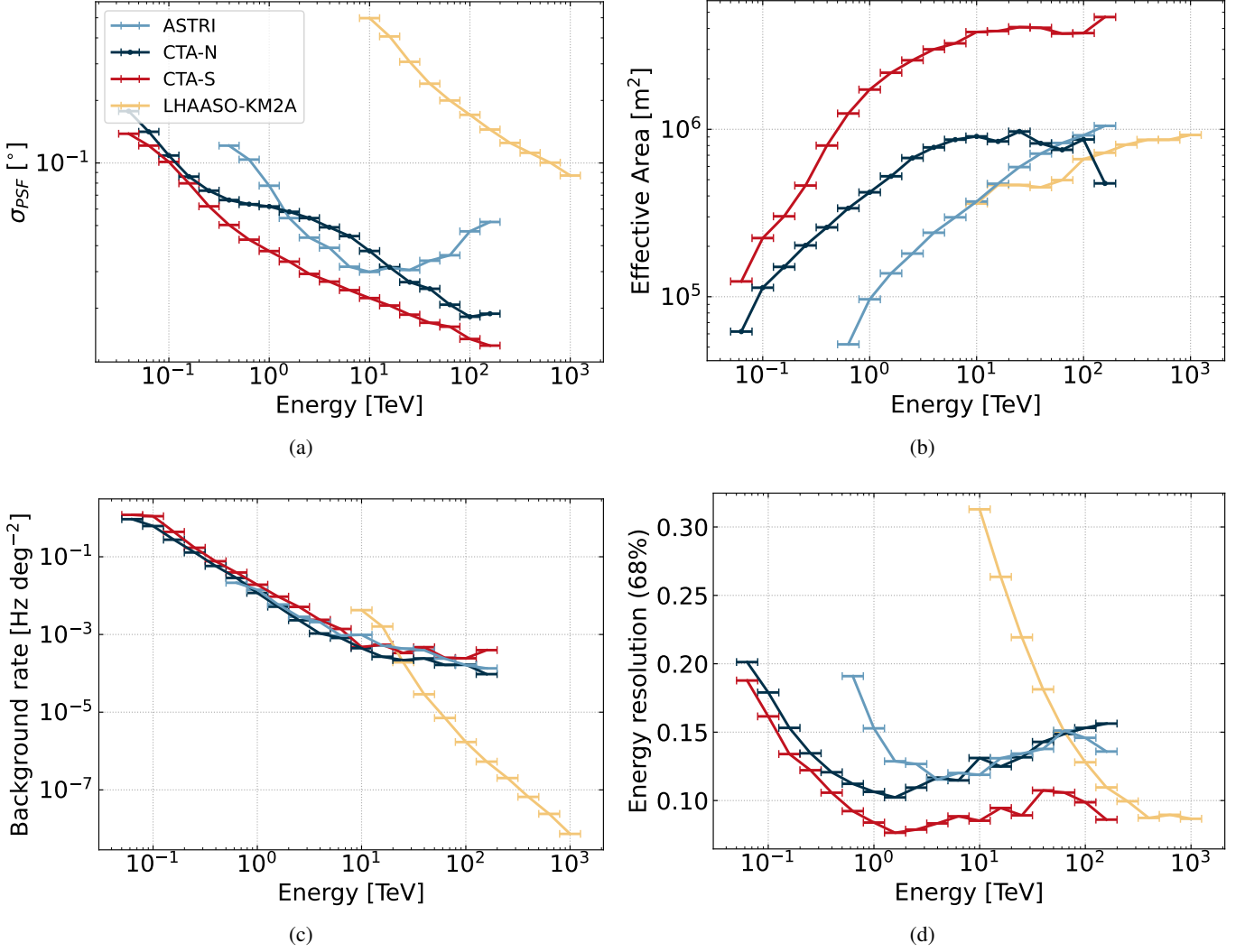


Fig. 1. Comparison between IRFs of LHAASO-KM2A, and the on-axis ones of CTA (North and South) and ASTRI: (a) $1\text{-}\sigma$ width of the PSF approximated as a Gaussian distribution. (b) effective area, (c) background rate, and (d) energy resolution. The drop observable in the last point of the CTA-N effective area is an artifact of the simulations, resulting from a statistical fluctuation.

obtained after the gamma/hadron separation cuts, while no selection relative to the reconstructed event direction was applied³.

4. Sensitivity studies towards extended sources

The careful evaluation of the instrument sensitivities is important for obtaining a clear understanding of the expected performance and discovery potential, as discussed for ground-based telescopes by Aharonian (1991). We here calculate differential sensitivities for extended sources of different instruments following the approach described in Ambrogi et al. (2018). Namely, we identify the minimum detectable flux that guarantees the following conditions to be satisfied in each energy bin of the computation (Bernlöhr et al. 2013), namely:

- 1) a minimum number of signal events, $N_s^{\min} = 10$;
- 2) a minimum significance detection level, $\sigma_{\min} = N_s / \sqrt{N_b} = 5$;
- 3) a minimum signal excess over the background, $N_s^{\min} / N_b = 0.05$.

³ <https://doi.org/10.5281/zenodo.5499840>

The number of signal events N_s expected per energy bin is obtained by folding the gamma-ray effective area with the Crab nebula spectrum⁴. However, it should be noted that the final sensitivity computation is independent of the assumed source flux. The number of background events N_b is computed from the background rate, assumed to be constant in time. While the background rate is directly provided in IACT IRFs, in the case of LHAASO we convolved the expected background flux with the effective area calculated for hadrons, namely after the implementation of CR rejection cuts such that only residual background is accounted for. For the significance σ we here adopt the definition given by Li & Ma (1983), with $N_{\text{on}} = N_s + N_b$ and $N_{\text{off}} = N_b / \alpha$, α being the ratio of the on-source to the off-source exposure; for our calculations, we assume $\alpha = 1$.

In each energy bin, the instrument sensitivity is limited by the one condition among the three listed above which dominates over the other two. As already discussed in (Ambrogi et al. 2018), we find that source detection is determined by the sig-

⁴ This is described in the TeV regime as a power-law function, $F_0 E^{-\alpha}$, where $F_0 = 2.83 \times 10^{-11}$ (TeV cm² s)⁻¹ is the flux normalization at 1 TeV and $\alpha = 2.62$ (Aharonian et al. 2004).

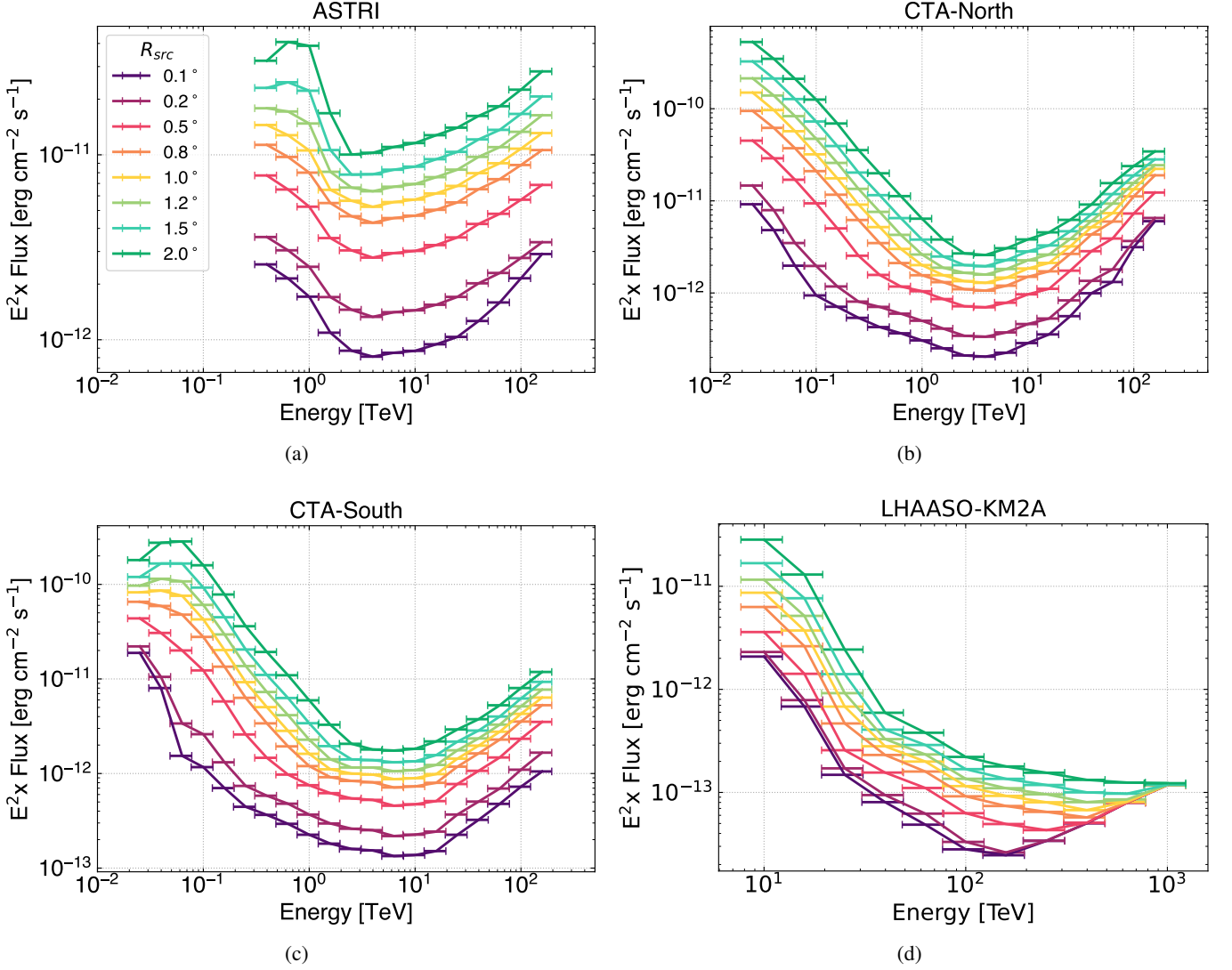


Fig. 2. Differential sensitivity towards the observation of extended sources by: (a) ASTRI, (b) CTA-N, (c) CTA-S, and (d) LHAASO. The exposure time adopted is 50 h for IACTs and 1 year for LHAASO. The source considered has a uniform disk-like morphology, whose angular radius is indicated in the legend.

nal over background ratio at low energies, by the significance condition in the intermediate energy range (i.e. close to the sensitivity minimum), and by signal event counts at the highest energies where the statistics becomes low. Since we require all the above criteria to be satisfied in each energy bin, a differential 5σ requirement corresponds to an actual higher significance in the energy bins where this is not the dominant condition (normally at the lowest and highest energies, respectively). Concerning the condition on the background uncertainty, for all detectors we assume a 1% accuracy on the modeling (and hence subtraction) of the residual background and require a signal excess of at least five times this background systematic uncertainty, i.e. $N_s/N_b \geq 0.05$, following the approach adopted by ASTRI and CTA (Cherenkov Telescope Array Consortium et al. 2019).

Moreover, to account for the statistical fluctuations of the background, the number of background events is randomly extracted from a Poissonian distribution with mean value N_b , and the result shown is averaged over 1000 realizations of the sensitivity estimation. Given the different observation strategy of the instruments, a benchmark observation time of 50 h is assumed for all IACTs while 1 year is considered for LHAASO, unless other-

wise specified. Furthermore, IRFs at an average zenith angle of 20° are used for the calculation of the extended source sensitivities, given that public IRFs are available for all the observatories under investigation specifically at this value. The effects of IACT observations at different zenith angles are discussed in Appendix B. We consider here disk-like sources with eight different radial sizes, i.e. $R_{src} = [0.1, 0.2, 0.5, 0.8, 1.0, 1.2, 1.5, 2.0]^\circ$; the choice of these specific sizes is mostly driven by an analog computation in our previous publication, see (Ambrogi et al. 2018). The instrument PSF affects the effective radius in which the signal is spread (R_{ON}), which we calculated as the convolution between the image of the source, described as a disk of radius R_{src} , and the PSF, assumed to be a Gaussian function with σ_{PSF} its standard deviation. Note that σ_{PSF} depends on energy (see Fig. 1a), and consequently also R_{ON} . For IACTs, the IRFs further depend on the offset from the center of the camera, as described in Appendix A. In order to account for the variation of performance across the FoV, we construct for each IRF a data cube, namely defining the corresponding value at each energy (E) and position (x,y) in the FoV. The source flux is analogously binned, with an energy dependence given by the spectral as-

sumption. We proceed then with the determination of R_{ON} by convolving the image with the PSF, considering the proper kernel $\sigma_{\text{PSF}}(x, y, E)$ for each point of the grid. We then compute the number of signal and background counts expected within R_{ON} by considering a weighted average of the effective area inside the on-region. With respect to the approach previously implemented in Ambrogi et al. (2018), this method allows us to account for the degradation of IRFs across the FoV and also to extend the computation to off-axis sources, i.e. centered at given distance R_{off} from the center of the FoV. We discuss this point further in Appendix A, where we also present differential sensitivities at different offsets in Fig. A.4.

4.1. Comparisons of sensitivities among different instruments

Our results indicate that the differential sensitivity strongly depends on the source extension, as it can be seen from Fig. 2. The worsening due to the source extension for all IACTs is found to be about one order of magnitude for most of the investigated sizes, while it remains more contained for KM2A, as expected due to its larger angular resolution. We also note that LHAASO-KM2A achieves a truly background free detection regime at energies above 1 PeV, as demonstrated by the convergence of sensitivity lines computed for different source extensions (see Fig. 2d). On the other hand, the degradation due to the offset is restrained to a factor of a few units for all IACTs, as shown in Fig. A.4. A comparative evaluation of the impact of these two effects (source extension and offset) is provided in Fig. 3, where the sensitivities computed for different extensions (R_{src}) and at different offsets (R_{off}), for IACTs, are compared to the sensitivity towards observations of a point source at the center of the camera ($R_{\text{src}} = R_{\text{off}} = 0^\circ$). Interestingly, ASTRI sensitivity is almost unaffected by the offset, mainly because of the small variation of its IRFs across the FoV, as it can be seen in Fig. A.1. This guarantees the possibility of studying multiple sources in the same pointing without losing much in performance.

To test our methods, we compared our calculations with the sensitivity for point-like sources calculated by the CTA and ASTRI collaboration, finding consistent results (see Appendix C and Fig. C.1). A consistency check among the resulting LHAASO-KM2A sensitivity and the sources listed in its first catalog can be performed, shown in Fig. 5b and further discussed later on.

5. Science cases

IACT and EAS measurements are complementary in many aspects: the former allow us to carry out precise spectroscopic and morphological studies of sources thanks to their superior energy and angular resolutions, while the large duty cycle and field of view of EAS arrays enable the deepest exposure to sources. The combination of these features will permit to investigate with an unprecedented level of accuracy some of the most relevant key science cases for the community. Specifically, the following developments are expected:

i) The improved angular resolution of IACTs will enable us to precisely locate the regions where particle interactions take place, within or around the accelerator, thus revealing information about the nature of the interaction itself (e.g. the presence of correlated emission with dense gas regions hints towards hadronic collision origin). This will further allow us to understand sources remaining unidentified in current VHE and UHE catalogs, as the first LHAASO catalog (Cao et al. 2023) or in the H.E.S.S. Galactic Plane Survey (HGPS), both of which

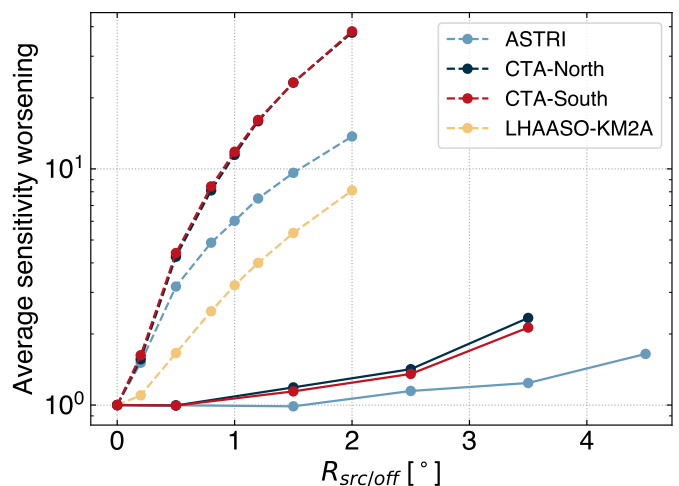


Fig. 3. Worsening of the differential sensitivity averaged for energies >1 TeV for IACTs and >10 TeV for LHAASO as a function of the source extension ($R = R_{\text{src}}$, dashed lines) and of the offset ($R = R_{\text{off}}$, solid lines). The worsening is expressed as the ratio between the calculated sensitivity and the on-axis point-like source sensitivity.

are discussed in Sec. 5.1.

ii) The improved energy resolution will be a key feature to investigate the cut-off region of energy spectra, containing information about in-situ acceleration, propagation and radiation properties of the primary particles producing the gamma rays (Celli et al. 2020). A careful analysis of the cut-off region is of paramount importance in the PeVatron search, particularly with regards to the hadronic PeVatrons responsible for the CR flux observed at Earth, as we discuss in Sec. 5.2.

iii) The large FoV of the next-generation IACTs will further allow us to better constrain the background around sources, facilitating the detection and the characterization of low-surface brightness sources such as molecular clouds, discussed in Secs. 5.3. Together with the improved angular resolution, this will permit to better model particle propagation around their sources: e.g., we expect the source size to change in energy in a leptonic scenario because of energy losses, as e.g. observed in the case of gamma-ray observations of the microquasar SS443 (MAGIC Collaboration et al. 2018; Abeysekara et al. 2018), while in hadronic scenarios the most energetic particles will travel loss-free to a further distance before interacting. An application of the propagation and escape concept certainly concerns Pulsar Wind Nebulae (PWNe) and their surrounding TeV halos (Giacinti et al. 2020), as we discuss in Sec. 5.4.

5.1. Catalogs follow-ups

Currently, both the HGPS (H. E. S. S. Collaboration et al. 2018) and the first LHAASO source catalog (Cao et al. 2023) contain more than half unidentified sources, requiring follow-up studies with improved-performance instruments. In these regards our calculations provide a clear assessment regarding the detection potential of each instrument and the time required to achieve a significant detection. We therefore proceed to the exploration of the two aforementioned source catalogs, in order to establish the most promising targets for each observatory.

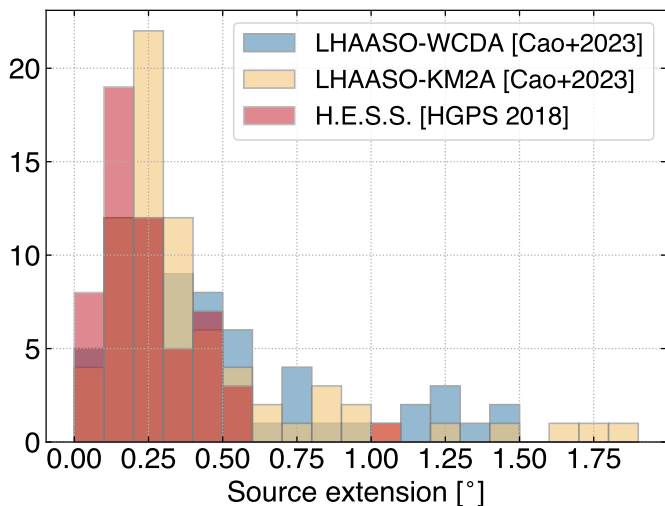


Fig. 4. Distribution of the extension of the sources included in the HGPS (H. E. S. S. Collaboration et al. 2018) and in the first LHAASO source catalog (Cao et al. 2023).

5.1.1. The first LHAASO source catalog

After the announcement of the first 12 sources (Cao et al. 2021), a new catalog was recently published by the LHAASO Collaboration (Cao et al. 2023), reporting on the observation of 90 sources of both Galactic and extra-galactic nature. Among these, 32 represent new discoveries and 43 emitters are detected in the UHE domain with a test statistics (TS_{100}) above 20 at 100 TeV: these sources are labeled with the letter u in Cao et al. (2023). The first LHAASO catalog was obtained by analysing the WCDA and KM2A data-sets separately, and only 54 sources are significantly observed by both instruments. The differential spectra measured by the two instruments are fitted independently, each with a power-law shape and the best-fit parameters are reported in the catalog. Although a tentative association is proposed in Cao et al. (2023), the large extensions (see Fig. 4) and superposition of sources, together with a poor understanding of the diffuse emission at such high energies, make the identification of the sources challenging. IACTs will at least partly compensate these issues, provided that a reasonable exposure will be guaranteed to detect source fluxes.

Thanks to the methods developed in this work, we are able to assess which of these sources can be effectively followed up, also accounting for the proper sensitivity worsening in case of extended objects. We show in Fig. 5 the differential fluxes of the catalogued LHAASO sources at 3 TeV and 50 TeV, provided respectively in the WCDA and KM2A catalogs, as a function of the measured source extension (Cao et al. 2023). We compared them to the sensitivity of future IACTs at the same energies and for different exposure times. The sources are further divided depending on their culmination zenith angles, where red and blue points in the figure represent sources that culminate at a zenith below 30° at the latitude of CTA-South and CTA-North (which is almost at the same latitude of ASTRI), respectively. With regards to WCDA sources, we find that almost all of the (so-defined) Southern sources will be accessible to CTA-South with 50 hr exposure, in line with the expectations. In fact, because the Southern sources fall at a higher zenith angle at the LHAASO site, a selection bias towards the brighter sources might be in place. In other words, because the LHAASO exposure is suppressed for sources observed at high-zenith angles

(Aharonian et al. 2021a), most likely only the brightest UHE sources in the Southern hemisphere are included so far in the LHAASO sample. Many of the Northern hemisphere sources will be seen by CTA-North and ASTRI with 50 hr exposure, and almost all with a longer exposure around 300 hr. With regards to KM2A sources, it appears that the extension of the sources might prevent in certain cases a clear detection with the considered observational setup. In particular, while many sources will be observed by CTA-South with 50 hr exposure, some will require a longer observation time, possibly up to ~ 300 h. Alongside, many of the detected KM2A-UHE sources will be detectable, allowing for a better characterization of these accelerators. Deep (300 hr) observations with ASTRI and CTA-North will also achieve a good-enough sensitivity to allow the follow-up of a handful of these interesting sources already in the next few years.

5.1.2. H.E.S.S. Galactic Plane Survey

The HGPS (H. E. S. S. Collaboration et al. 2018) is a survey performed by H.E.S.S. of the Galactic Plane ($65^\circ < l < 250^\circ$, $|b| \leq 3^\circ$) containing 78 sources, detected down to $\sim 1\%$ of the Crab flux. More than 60% of the sources are unidentified and $\sim 80\%$ are extended. Moreover, only for 15% of sources (12 objects) energy spectra are consistent with exponential cut-off power laws (a pure power law is fitted otherwise), revealing a maximum cut-off energy in the HGPS at 19.2 TeV. In these respects, it appears clear that observations with next-generation instruments, more sensitive than H.E.S.S. at energies ≥ 10 TeV, are needed in order to characterize the actual maximum energy achieved by these sources. While we expect CTA to improve the observations of basically all H.E.S.S. detected sources around 10 TeV, it is worth exploring the capability of next-generation IACTs in following up HGPS sources at higher energies. Despite the sky coverage of the Northern observatories and H.E.S.S. is not identical, a few sources are visible from both hemispheres, although culminating at different zenith angles depending on the site. In Fig. 6, we show the HGPS source fluxes at 10 and 50 TeV as a function of the corresponding extension. Note that flux values at 50 TeV are obtained by extrapolating the given spectral slope in the assumption of a pure power-law or an exponential-cutoff power-law with the tabulated parameters for each source. We also show the sensitivity of ASTRI for different exposures at a fixed zenith angle of 20° and those of the two CTA observatories with 300 hr observations in a range of zenith angles between 20° and 60° , represented by a band. Further details about the expected CTA sensitivities with varying zenith are provided in Appendix B, showing that above few tens of TeV an improvement of about a factor 2 can be achieved in high-zenith angle observations, similarly to what was demonstrated in the case of MAGIC (Sommers & Elbert 1987; Konopelko et al. 1999; MAGIC Collaboration et al. 2020). We expect analogous considerations to hold for ASTRI, but lacking of the proper IRFs at different culmination angles, we limit the ASTRI discussion to low-zenith angles sensitivities. Moreover, we include a color scale indicating the zenith angle at culmination for each source at the latitude of ASTRI: in particular the scale takes a white color for high-zenith angle observations, meaning a less solid comparison with the sensitivity here shown. As a result of the comparison, we find that with a long enough exposure ASTRI will allow to investigate almost the entire HGPS sample at 10 TeV. Similarly, good prospects are also expected for 50 TeV observations, where more than half of the sources will be in the reach of both ASTRI and CTA.

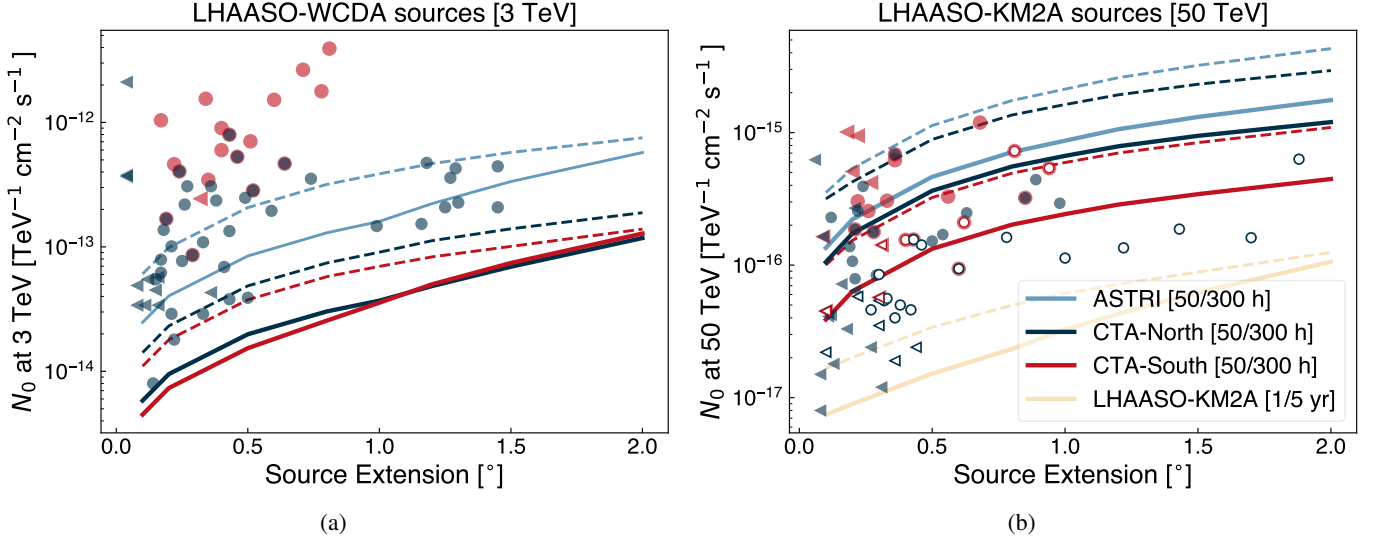


Fig. 5. Differential flux of LHAASO first catalog sources as a function of their radius, measured (circles) or upper limits (triangles), as evaluated by WCDA at 3 TeV (a) and KM2A at 50 TeV (b). Color code refers to culmination at zenith angles below 30° at each observatory sites (red for CTA-South, blue for CTA-North and ASTRI). Filled markers in the right panel correspond to UHE sources in LHAASO first source catalog (with test statistics at 100 TeV $TS_{100} > 20$). Lines show the ASTRI and CTA differential sensitivities as a function of the source extension; dashed for shorter observation time and solid for the longer one, as indicated in the legend.

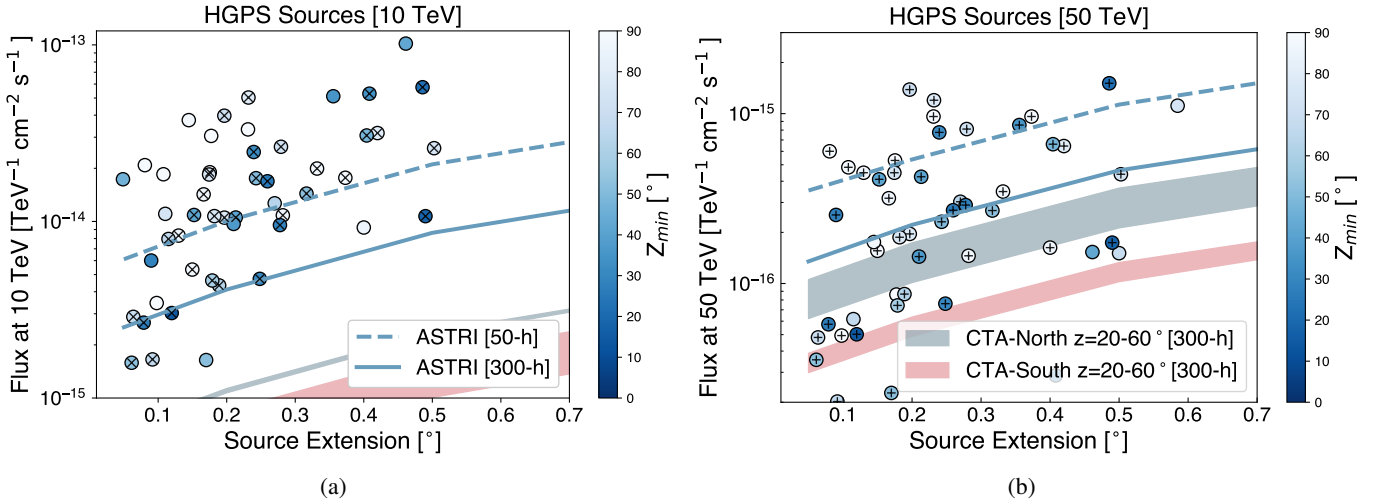


Fig. 6. HGPS (H. E. S. S. Collaboration et al. 2018) source fluxes (markers) as a function of their extensions at (a) 10 TeV and (b) 50 TeV, compared to the differential sensitivities (lines) of ASTRI and CTA for different exposures. The latter are evaluated at a zenith of 20° for ASTRI, whereas in the case of CTA we span different zenith angles up to 60° with a band. In the right panel, source fluxes are extrapolated up to 50 TeV by assuming a power-law or and exponential cutoff power-law spectrum, according to the indication of the HGPS catalog. Sources marked with a grey cross in the left panel are unidentified ones, while a plus marker to the right indicates sources without any detected cut-off by H.E.S.S.. The color code indicates the culmination zenith angle of sources at the ASTRI location, corresponding approximately to that of CTA-N. Note that low-zenith angle observations with CTA-N correspond to high-zenith angle observations with CTA-S.

5.2. Identifying hadronic PeVatrons

Currently there are two different concept of PeVatrons in the community, one intended to address theoretically the first-principle question about the origin of CRs at the knee, and the other given from the observational perspective to describe sources showing signatures of PeV particles regardless of their contribution to the CR spectrum itself.

In the particle acceleration framework, the exact value of the particle maximum energy achieved depends on the spectral shape of the accelerated particles: e.g., in the case of a power-law spectrum with exponential cut-off, the maximum energy corresponds

to the value where the flux deviates from the power law by $1/e$, while in the case of a sharp cut-off it basically corresponds to the drop itself. Two important considerations are: first, that the maximum particle energy inferred today in a given system does not necessarily coincide with the maximum energy ever produced by it. While it does for stationary accelerators, as the wind termination shocks of stellar clusters, in impulsive accelerators as Supernova Remnants (SNRs) the escape of particles might deprive the shocks of the highest energy particles at an early stage. Our current *in-situ* observations can then only catch the still confined particle population (see Celli et al. (2019)). Hence, the correct assessment of PeVatron activity of a given system can only be

achieved through dedicated models, and not simply by spectral fitting. Second, a further constraint for the CR PeVatron scenario concerns the slope of the injection spectrum, that is required to be between 2.2 and 2.4 to reproduce the *local* observations⁵.

The other definition, in turn, deals with the experimental signatures of PeVatron activity, e.g. the emission of UHE photons in the hadronic collisions of PeV protons and nuclei. On average, the ratio between the primary proton energy and the secondary gamma rays amounts to about a factor 10 across the spectral energy distribution, with the exception of the cut-off region, that in secondary particles appear milder than in primaries (Celli et al. 2020). As such, it is not sufficient to detect 100 TeV gamma rays to claim the presence of a PeVatron, rather the hadronic nature of the observed radiation should be probed and its spectral shape well sampled. To this extent, high-resolution spectral and angular observations are of paramount importance, and will be available with next-generation IACTs.

So far, LHAASO observations have revealed a few SNRs (Cao et al. 2023), characterised by featureless energy spectra and slopes significantly steeper than E^{-2} in the UHE band. Nonetheless, in order to clearly assess the overall spectral trend of the emission and probe the physics of the source, it appears necessary to perform broadband fits, rather than being limited to the energy range of individual observations. In fact, identifying the presence of a cut-off or any other spectral variation would be crucial to the PeVatron science case: e.g. a cut-off might indicate either a drop in the available source power or the dominance of energy losses, depending on its shape, while an energy break might result from the occurrence of particle escape from the accelerator (Celli et al. 2019; Morlino & Celli 2021). In summary, current measurements at the highest energies are still affected by large uncertainties to draw conclusive statements, requiring the collection of increased statistics and multi-wavelength analysis. In these regards, improved energy resolution will also be a key feature of future IACTs, possibly providing the resolving power to clearly identify spectral features at the highest energies.

The list of LHAASO detected sources include many objects showing significant emission > 100 TeV, possibly competing to be hadronic PeVatrons. The only clear identification so far concerns the Crab Nebula, mostly dominated by leptonic emission. However, a hint for a spectral hardening at the highest energies probed by LHAASO suggests an additional component possibly be due to hadrons (Nie et al. 2022). The confirmation of this scenario awaits improving mapping of the emitting region at these extreme energies.

It is hence of primary importance to investigate which source can be detected at 100 TeV by the next-generation IACTs. To do that, we extrapolate the flux reported from KM2A observations up to 100 TeV: in Fig. 7 we compare the resulting flux, F_{100} , to the differential sensitivity of ASTRI and CTA. In particular, the left panel refers to observations at 20° zenith angles, while the right panel concerns high-zenith angle (60°) observations for CTA only. As it emerges from our estimation, CTA-South has the potential for investigating several objects at 100 TeV; among these, the source powering the region of 1LHAASO 1825-1337u and 1LHAASO J1809-1928u, possibly linked to pulsar emission (Cao et al. 2023), will be potentially visible already with a short 50-hour exposure. A deeper exposure coupled to high-zenith angle observations will enable all observatories to access a larger number of sources, despite their extensions.

⁵ Note that the injection spectrum does not necessarily correspond to the particle acceleration spectrum (see (Celli et al. 2019) for a detailed treatment concerning SNRs).

5.3. Molecular clouds

Molecular clouds (MCs) illuminated by CRs constitute a class of Galactic gamma-ray emitters, typically detected in the GeV energy range (Aharonian et al. 2020; Peron et al. 2021; Baghmany et al. 2020). These are compact ($\sim 10 - 100$ pc) regions of enhanced gas density ($n \sim 10 - 100 \text{ cm}^{-3}$) recognizable in the surveys of CO ($J=2 \rightarrow 1$) line (Dame et al. 2001). When high-energy CRs impact the clouds, they produce (among other secondaries) gamma radiation proportional to both the density of the target gas and that of CRs, making MCs the most straightforward tracers of CRs far from the Earth.

In the following, we evaluate the cloud visibility in the multi-TeV energy range. We consider the MCs listed in the catalog of Miville-Deschênes et al. (2017) as passive target for the local CR flux, and compare the expected gamma-ray flux emerging from hadronic collisions with the sensitivity of next-generation instruments, accounting for the cloud extension and the column density reported in the catalog. Following Peron & Aharonian (2022), we compute the resulting photon flux by assuming the locally measured CR flux $J_\odot(E_p)$ (Orlando 2018; Lipari & Veronetto 2020), as:

$$F_\gamma = n_{\text{col}} d\Omega \xi_N \int dE_p \frac{d\sigma}{dE_\gamma} J_\odot(E_p) \quad (1)$$

where n_{col} is the cloud column density, $d\Omega$ is the angular area covered by the cloud, ξ_N is the nuclear enhancement factor accounting for metals in both the CRs and the target gas, and $d\sigma/dE_\gamma$ is the inelastic proton-proton differential cross section (Peron & Aharonian 2022). The assumption that the same CR spectrum across the Galaxy illuminates the clouds implies that the resulting hadronic gamma-ray flux only depends on their mass and distance. Indeed $F_{\text{cloud}} \propto n_{\text{col}} d\Omega = M/d^2$, in specific units. Following (Aharonian et al. 2020), we define $A = M_5/d_{\text{kpc}}^2$ as the ratio between the cloud mass (scaled to 10^5 solar masses) and the squared distance (in kpc units), and factorize the flux as $F_\gamma(E) = A\phi_\gamma(E)$, being $\phi_\gamma(E)$ the emissivity per single hydrogen atom. As a consequence, the visibility condition translates into a mere constraint regarding A : defining the instrument sensitivity for given source extension as $S_{\text{min}}(E, R_{\text{src}})$, then

$$F_\gamma(E) > S_{\text{min}}(E, R_{\text{src}}) \rightarrow A > S_{\text{min}}(E, R_{\text{src}})/\phi_\gamma(E). \quad (2)$$

In Fig. 8 we compare the A parameter characterizing the catalogued MCs to the ratio between sensitivity and emissivity at various energies and exposures. Also in this case, the zenith angle at which the cloud is observed might also influence the detection, especially at low energies. We consider here only the case of low-zenith angle observations ($< 20^\circ$), and we indicate through the color code in Fig. 8 the zenith angle at which the clouds culminate at the Southern and Northern sites of CTA, the latter being located approximately at the same latitude as ASTRI and LHAASO. As it can be seen from the plot, the clouds with highest A culminate at lower zenith angles in the Southern hemisphere, resulting in a possible detection of a few targets already with a 50-hour exposure by CTA-S. In Northern sites, on the other hand, the same clouds culminate at high-zenith angles, where observations are characterised by an increased energy threshold (see Appendix B). This is however limiting the prospects for the observation of the molecular clouds that are illuminated by the local CRs only, because a steep gamma-ray emissivity is expected in this case. Concerning LHAASO, only a few clouds are found to be possibly detectable with a 10-year

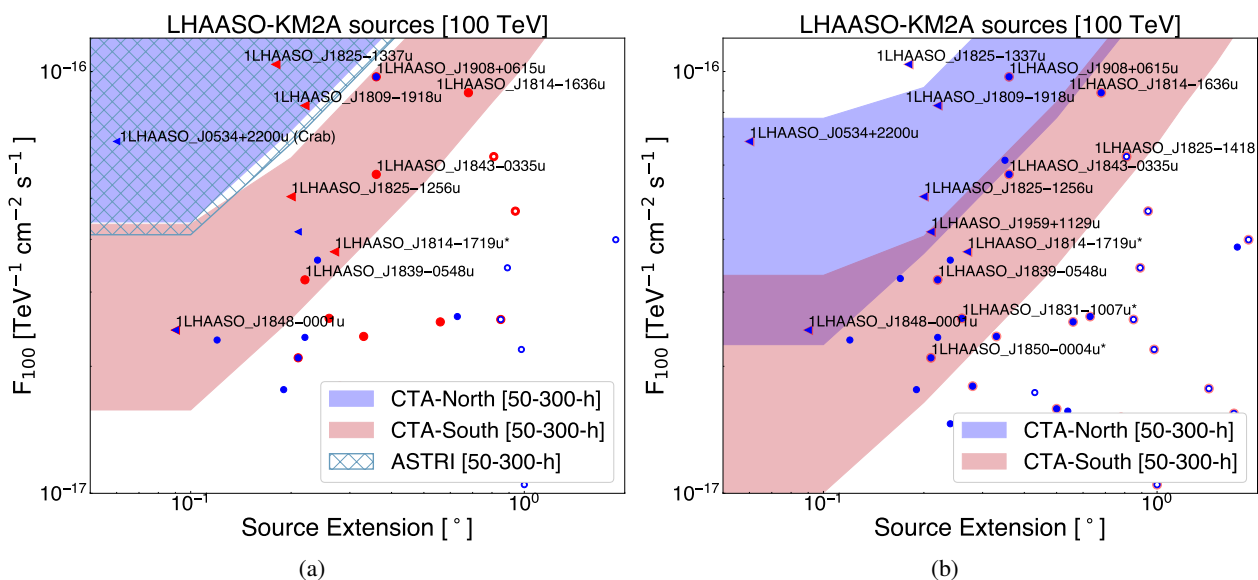


Fig. 7. Expected gamma-ray flux at 100 TeV from the LHAASO-KM2A source sample, as computed by extrapolating the spectral fits provided in Cao et al. (2023). UHE sources as identified in LHAASO-KM2A catalog ($TS_{100} > 20$) are shown in solid markers, while empty markers represent the remaining sample; visible sources by any IACT are labeled in the plot. Overlaid are shown the differential sensitivities of ASTRI and CTA, where the bans span different exposure times from 50 to 300 hours. *Left:* The differential sensitivity is calculated with minimum zenith angle of sources equal to 20° . *Right:* Sensitivities are calculated for minimum zenith angle of 60° ; ASTRI is not included in this panel as its IRFs in such conditions are not yet available for this study.

long exposure. As a consequence, our result clearly suggests that passive MCs illuminated by the CR sea cannot be responsible for the unassociated sources in the first LHAASO catalog (Cao et al. 2023), which is based on a 933-day long exposure. However, future detection of MCs could enable to probe the Galactic CR spectrum up to > 100 TeV, which is a particularly interesting energy range because of the discrepant results currently shown by ground-based measurements (Aartsen et al. 2019).

Nevertheless, one should consider that a large level of enhancement in the CR flux can be reached in the proximity of accelerators, due to the escaping particles (Aharonian & Atoyan 1996; Gabici & Aharonian 2007). E.g., the scenarios where Galactic clouds could be illuminated by SNR and YMSC escaped particles were studied in great details by Mitchell et al. (2021) and Celli et al. (2023), respectively. Furthermore, many among the clouds observed in gamma rays showed an enhancement as large as ~ 5 compared to *local* (i.e. at Earth) cosmic-ray measured flux, even if not directly associated with an accelerator: such enhanced emissions from clouds were found mostly in the inner part of the Galaxy (Aharonian et al. 2020), but also in the local ($\lesssim 2$ kpc) medium (Baghmanyan et al. 2020; Peron & Gabici 2023). Similar enhancements would dramatically increase the detectability, allowing us to probe cloud spectra even at high energies, as done e.g. by the H.E.S.S. Collaboration (Sinha et al. 2021) for one of such systems, namely cloud 877 from the Rice et al. (2016) catalog. The extension of these type of observations to other objects, although challenging, would be of extreme relevance to probe the CR density elsewhere in the Galaxy especially at high energies, where a clear picture is not yet.

5.4. PWNe and pulsar halos

A new source class, named Pulsar/TeV halos, has emerged recently in the VHE surveys of the large FoV instrument HAWC. These sources are found in correspondence of pulsars, despite being much more extended than the associated surrounding

PWN, therefore interpreted as a halo of particles escaping from the nebula. Interestingly, LHAASO observations have revealed that 40% of the first catalog sources are coincident with pulsars, possibly powerful enough to support UHE emission (de Oña Wilhelmi et al. 2022).

The first detection of such objects was obtained in the direction of the Geminga and Monogem pulsars (Abeysekara et al. 2017a): around these pulsars, a $\gtrsim 2^\circ$ halo was measured by HAWC, corresponding to a distance of about 50 pc from the central compact object. Current IACT observations are limited by the extension of such halos, covering (and often going beyond) their entire FoV as in the case of Geminga (H. E. S. S. Collaboration et al. (2023)), representing a noticeable analysis challenge for the background estimation. Furthermore, significant flux differences have emerged in current measurements from IACTs and EASs of several sources because of the different integration region, making the case for observations with large FoV IACTs, like ASTRI, more compelling than ever.

Interestingly, in order to explain the halo emission, a strong suppression of the diffusion coefficient is required, with strong implications regarding the amount of CR positron produced by these sources and in general on the propagation of Galactic CRs (López-Coto et al. 2022). However, Monogem and Geminga are found in the same region, therefore a local deformation of the magnetic field, which would impact the diffusion of particles regardless of the presence of the pulsars, cannot be excluded a priori. Despite this hypothesis being disfavoured theoretically (De La Torre Luque et al. 2022), further observations are necessary to conclude about the origin of the observed halos and to which extent they can influence the diffusion properties of the interstellar medium.

At the moment, it is not clear whether these sources are the only pulsar halos in the sky or if any other exists, although some evidence for similar phenomena emerged in the most up-to-date catalogs of TeV sources. One candidate pulsar halo is the source HESS J1825-137, because its extension appears sig-

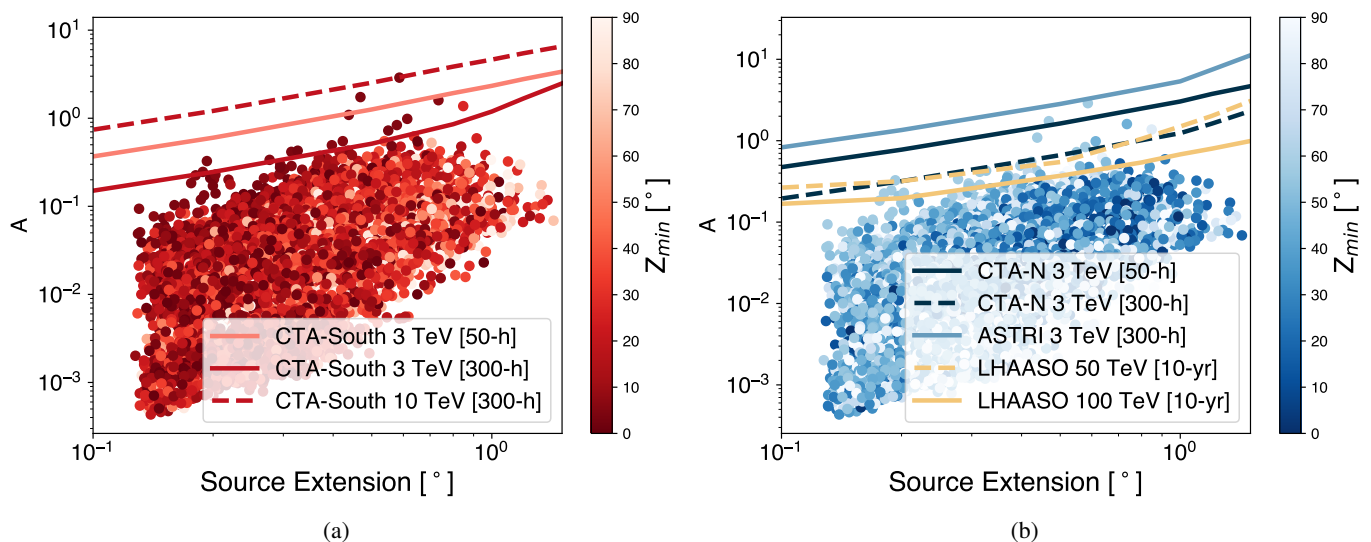


Fig. 8. Detectability of molecular clouds in terms of their A parameter and extension (Miville-Deschênes et al. 2017). The sensitivity of the various instruments at different energies are normalized to the expected cloud emissivity at the same energy (see text). The left panel refers to CTA-S, while the right panel to Northern observatories. The same cloud sample is reported in the two panels. The color scale refers to the minimum zenith angle for the clouds at each location.

nificantly larger than ordinary PWNe, suggesting that escape must be taking place from the nebula. Another candidate is LHAASO J0621+3755, one of the first sources detected in UHE gamma rays, its morphology being compatible with the scenario of escaped particles as claimed in Aharonian et al. (2021b). The observations with LHAASO-KM2A point towards a suppression of the diffusion coefficient to a similar level as measured in Geminga and Monogem. Again, high resolution spectral and morphological observations would be crucial for confirming the nature of this accelerator. Other candidate TeV halos have been announced by the HAWC collaboration, namely HAWC J0543+233 and HAWC J0635+070, both included in the second HAWC catalog (Abeysekara et al. 2017b): also in these cases, further morphological and spectral characterization are needed to be confirmed as halos, as current measurements could not resolve the radial profile of the emission neither the energy cut-off region with sufficient accuracy. All of these sources are expected to be powered by middle-age pulsars ($\gtrsim 100$ kyr). An exception is found in the pulsar of Vela, namely Vela X: Vela shows a dim extended emission detected both in radio and in the high-energy range, which is often interpreted as “relic PWN”, left behind after the interaction of the expanding PWN and the SNR reverse shock. The extension of the emission is however compatible also with a TeV halo scenario, making Vela X a possible intermediate case between the relic and the halo phase (Giaccinti et al. 2020). Similarly, a TeV halo interpretation has been suggested to explain the extended emission detected by HAWC around the young pulsar PSR J0359+5414 (Albert et al. 2023). Furthermore, the aforementioned pulsar does not show a radio counterpart, analogously to the case of LHAASO J0621+3755. If this association is confirmed, it would imply that a larger variety of pulsars, compared to the present understanding, is able to produce halos. For these candidates, we provide in Fig. 9 a comparison between their differential fluxes and the calculated sensitivity of future IACTs and LHAASO for a 0.5° extension, compatibly with their reported sizes in TeVCat⁶ and reported in the figure legend. The selected sources will be possibly vis-

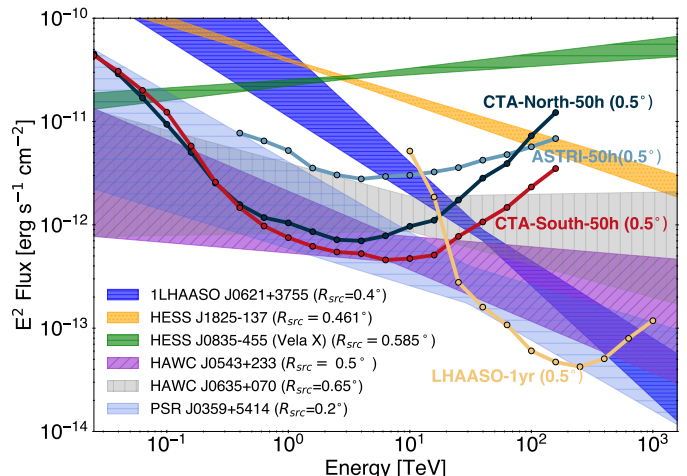


Fig. 9. Differential flux of the candidate TeV halos discussed in the text, compared with the sensitivity for extended ($R_{\text{src}} = 0.5^\circ$) sources of the next-generation IACTs. The measured size of each source is also reported in the legend, as extracted from TeVCat. The shaded bands are computed from the 1σ spectral uncertainties (slope and normalization) also provided there.

ible with the benchmark exposures by the planned instruments, therefore allowing a comprehensive characterization of the emission around these pulsars, that so far is still missing. Investigating with high resolution the spatial profile of the flux of run-away particles might yield insight into radially-dependent diffusion properties. Such a goal is expected to be achieved in the future: in fact, the limited performance worsening when moving away from the axis center (Figs. A.1, A.2, A.3, and A.4) can be favourably exploited in such an application. We therefore expect high quality results in this field, although a more detailed evaluation needs to be performed to quantify the detectability of very large emitting regions as Geminga, e.g. accounting for the exact source geometry and spatial dependency of the spectrum.

⁶ <http://tevcat.uchicago.edu>

6. Conclusions

The highest energy window ever probed in gamma-ray astronomy has recently been opened by LHAASO observations, reporting extended and often complex emitting regions located in the Plane of the Galaxy. The limited angular resolution of EAS arrays has so far impeded the clear identification of the nature of these objects, which represents one of the next major goals of the VHE community. Improved morphological measurements by next-generation IACTs are expected to reduce source confusion from nearby objects. At the same time, lowering the angular resolution will allow us to perform significantly better correlation studies between gamma-ray and multi-wavelength data, which are very relevant to unveil the origin of the gamma radiation. Moreover, accurate spectral analyses might provide further insights into the physical mechanisms at the origin of the radiation. Joint analysis of IACTs and LHAASO data will help in reducing spectral uncertainties, thus improving the modeling.

In order to get a realistic evaluation of IACT detection prospects and required exposure times with regards to known extended gamma-ray sources, we have performed a comparative analysis of ASTRI, CTA, and LHAASO. Starting from their expected performances, we defined a method to obtain differential sensitivities towards the observation of extended sources. We found minimum detectable fluxes at the level of 10^{-12} erg cm $^{-2}$ s $^{-1}$ for 50 hr exposure by CTA-N (at 3 TeV), 5×10^{-13} erg cm $^{-2}$ s $^{-1}$ for 50 hr exposure by CTA-S (at 8 TeV), 3×10^{-12} erg cm $^{-2}$ s $^{-1}$ for 50 hr exposure by ASTRI (at 3.5 TeV), and 6×10^{-14} erg cm $^{-2}$ s $^{-1}$ for 1 yr exposure by LHAASO (at 100 TeV), all evaluated with disk-like sources of angular radius equal to 0.5° and at 20° zenith angle observations. We have further explored the expected IACT detection improvements for high zenith angle observations at the highest energies.

Since our analysis relies on publicly available IRFs provided by each collaboration, our method to assess the sensitivity for extended sources does not include any optimization of the tools for reconstruction of the properties of primary particles, neither of dedicated background rejection methods. A precise estimation of the instrument capabilities for the detection of extended sources would require a complete 3D analysis: particularly for IACTs, the study of sub-structures on arcminute scales would permit to resolve the morphological details of many extended sources beyond the disk-like structure considered here. Moreover, we considered a single shape for the source, a uniform disk, but our methods can in principle be extended to any source morphology, including the case of asymmetric shapes for which we expect some differences as a consequence of non-uniform responses of the instruments across the FoV. Future studies will deal with the contamination of nearby sources as well as the determination of the contribution of the Galactic diffuse emission as an additional background source.

Our investigation enabled us to identify the most promising extended targets, considering both the first LHAASO catalog and the HGPS, to be observed with the next generation of IACTs. We remark that the detection assessment here derived should be regarded as quite conservative, because it resulted from considering region of interests of the same extent as that announced by LHAASO; on the other hand, if the actual source size were smaller than claimed, a detection from IACTs may require a shorter exposure than what estimated here. In particular, IACTs are expected to be sensitive to emission peaks, that might be spread out in EAS observations.

We discussed specific key science cases to resolve: i) candidate PeVatrons, potential CR sources; ii) passive molecular

clouds, potential gamma-ray unidentified sources; and iii) TeV halos, a novel class recently observed in gamma-ray astronomy. Additional studies with future IACTs might shed light on each of these open scientific questions.

Acknowledgements. This research has made use of the CTA instrument response functions provided by the CTA Observatory and Consortium, see <https://www.cta-observatory.org/science/cta-performance/> (version prod5 v0.1; <https://doi.org/10.5281/zenodo.5499840>) for more details, and of the ASTRI Mini-Array Instrument Response Functions (IRFs) provided by the ASTRI Project (ASTRI-Project 2022). The authors thank F. Aharonian, S. Gabici, E. Amato, C. Zhen, S. Zhang, C. Li, and W. Zha for fruitful discussions. SC acknowledges fundings from Sapienza University of Rome with grant agreement RG12117A87956C66. The research of GP was partly funded by Agence Nationale de la Recherche (grant ANR-21-CE31-0028). GP further acknowledges financial support from the INAF initiative "IAF Astronomy Fellowships in Italy". This paper went through the internal ASTRI and CTA review processes, for which we acknowledge comments from A. Giuliani, S. Lombardi, and M. Strzys that have improved the manuscripts.

References

- Aartsen, M. G., Ackermann, M., Adams, J., et al. 2019, *Phys. Rev. D*, 100, 082002
- Abeyssekara, A. U., Albert, A., Alfaro, R., et al. 2017a, *Science*, 358, 911
- Abeyssekara, A. U., Albert, A., Alfaro, R., et al. 2018, *Nature*, 562, 82
- Abeyssekara, A. U., Albert, A., Alfaro, R., et al. 2017b, *ApJ*, 843, 40
- Aharonian, F., Akhperjanian, A., Beilicke, M., et al. 2004, *apj*, 614, 897
- Aharonian, F., An, Q., Axikegu, et al. 2021a, *Chinese Physics C*, 45, 025002
- Aharonian, F., An, Q., Axikegu, Bai, L. X., et al. 2021b, *Phys. Rev. Lett.*, 126, 241103
- Aharonian, F., Bergström, L., & Dermer, C. 2013, *Astrophysics at Very High Energies: Saas-Fee Advanced Course 40*. Swiss Society for Astrophysics and Astronomy, Saas-Fee Advanced Course, Vol. 40
- Aharonian, F., Peron, G., Yang, R., Casanova, S., & Zanin, R. 2020, *Phys. Rev. D*, 101, 083018
- Aharonian, F. A. 1991, *Ap&SS*, 180, 305
- Aharonian, F. A. & Atoyan, A. M. 1996, *A&A*, 309, 917
- Albert, A., Alfaro, R., Arteaga-Velázquez, J. C., et al. 2023, *ApJ*, 944, L29
- Ambrogio, L., Celli, S., & Aharonian, F. 2018, *Astroparticle Physics*, 100, 69
- Antonelli, L. A. 2023, *PoS, ICRC2023*, 755
- ASTRI-Project. 2022, ASTRI Mini-Array Instrument Response Functions (Prod2, v1.0) (1.0) [Data set]. Zenodo. <https://doi.org/10.5281/zenodo.6827882>
- Baghmany, V., Peron, G., Casanova, S., Aharonian, F., & Zanin, R. 2020, *ApJ*, 901, L4
- Berge, D., Funk, S., & Hinton, J. 2007, *A&A*, 466, 1219
- Bernlöhr, K., Barnacka, A., Becherini, Y., et al. 2013, *Astroparticle Physics*, 43, 171
- Cao, Z., Aharonian, F., An, Q., et al. 2023, *arXiv e-prints*, arXiv:2305.17030
- Cao, Z., Aharonian, F. A., An, Q., et al. 2021, *Nature*, 594, 33
- Catalano, O., Capalbi, M., Gargano, C., et al. 2018, in *Society of Photo-Optical Instrumentation Engineers (SPIE) Conference Series*, Vol. 10702, Ground-based and Airborne Instrumentation for Astronomy VII, ed. C. J. Evans, L. Simard, & H. Takami, 1070237
- Celli, S., Aharonian, F., & Gabici, S. 2020, *ApJ*, 903, 61
- Celli, S., Morlino, G., Gabici, S., & Aharonian, F. A. 2019, *MNRAS*, 490, 4317
- Celli, S., Specovius, A., Mitchell, A., Morlino, G., & Menchiari, S. 2023, *PoS, ICRC2023*, 775
- Cherenkov Telescope Array Consortium, Acharya, B. S., Agudo, I., et al. 2019, *Science with the Cherenkov Telescope Array*
- Cherenkov Telescope Array Observatory & Cherenkov Telescope Array Consortium. 2021, CTAO Instrument Response Functions - prod5 version v0.1 (v0.1) [Data set]. <https://doi.org/10.5281/zenodo.5499840>
- Dame, T. M., Hartmann, D., & Thaddeus, P. 2001, *ApJ*, 547, 792
- De La Torre Luque, P., Fornieri, O., & Linden, T. 2022, *Phys. Rev. D*, 106, 123033
- de Oña Wilhelmi, E., López-Coto, R., Amato, E., & Aharonian, F. 2022, *ApJ*, 930, L2
- Dong, X., Li, C., & He, H. 2024, *arXiv e-prints*, arXiv:2401.01038
- Gabici, S. & Aharonian, F. A. 2007, *ApJ*, 665, L131
- Gaisser, T. K., Stanev, T., & Tilav, S. 2013, *Frontiers of Physics*, 8, 748
- Giacinti, G., Mitchell, A. M. W., López-Coto, R., et al. 2020, *A&A*, 636, A113
- H. E. S. S. Collaboration, Abdalla, H., Abramowski, A., et al. 2018, *Astronomy & Astrophysics*, 612, A1
- H. E. S. S. Collaboration, Aharonian, F., Ait Benkhali, F., et al. 2023, *A&A*, 673, A148

- Hillas, A. M. 1985, in International Cosmic Ray Conference, Vol. 3, 19th International Cosmic Ray Conference (ICRC19), Volume 3, 445
- Konopelko, A., Aharonian, F., Hemberger, M., et al. 1999, *Journal of Physics G Nuclear Physics*, 25, 1989
- Li, T.-P. & Ma, Y.-Q. 1983, *The Astrophysical Journal*, 272, 317
- Lipari, P. & Vernetto, S. 2020, *Astroparticle Physics*, 120, 102441
- Lombardi, S., Antonelli, L. A., Bigongiari, C., et al. 2022, in 37th International Cosmic Ray Conference, 884
- López-Coto, R., de Oña Wilhelmi, E., Aharonian, F., Amato, E., & Hinton, J. 2022, *Nature Astronomy*, 6, 199
- MAGIC Collaboration, Acciari, V. A., Ansoldi, S., et al. 2020, *A&A*, 635, A158
- MAGIC Collaboration, Ahnen, M. L., Ansoldi, S., et al. 2018, *A&A*, 612, A14
- Maier, G. & Knapp, J. 2007, *Astroparticle Physics*, 28, 72
- Mitchell, A. M. W., Rowell, G. P., Celli, S., & Einecke, S. 2021, *MNRAS*, 503, 3522
- Miville-Deschênes, M.-A., Murray, N., & Lee, E. J. 2017, *ApJ*, 834, 57
- Morlino, G. & Celli, S. 2021, *MNRAS*, 508, 6142
- Nie, L., Liu, Y., Jiang, Z., & Geng, X. 2022, *ApJ*, 924, 42
- Orlando, E. 2018, *MNRAS*, 475, 2724
- Peron, G. & Aharonian, F. 2022, *A&A*, 659, A57
- Peron, G., Aharonian, F., Casanova, S., Yang, R., & Zanin, R. 2021, *ApJ*, 907, L11
- Peron, G. & Gabici, S. 2023, *PoS, ICRC2023*, 683
- Rice, T. S., Goodman, A. A., Bergin, E. A., Beaumont, C., & Dame, T. M. 2016, *ApJ*, 822, 52
- Scuderi, S., Giuliani, A., Pareschi, G., et al. 2022, *Journal of High Energy Astrophysics*, 35, 52
- Sinha, A., Baghmany, V., Peron, G., et al. 2021, in 37th International Cosmic Ray Conference
- Sommers, P. & Elbert, J. W. 1987, *Journal of Physics G Nuclear Physics*, 13, 553
- Vercellone, S., Bigongiari, C., Burtovoi, A., et al. 2022a, *Journal of High Energy Astrophysics*, 35, 1
- Vercellone, S., Bigongiari, C., Burtovoi, A., et al. 2022b, *Journal of High Energy Astrophysics*, 35, 1

Appendix A: IACT worsening of IRFs with offset

In the case of IACTs, extended source sensitivity is further degraded with respect to that presented in Sec. 4 if observations are carried out off-axis. Reduced performance are expected both in angular resolution and effective area. A preliminary estimation of the differential sensitivity degradation for extended source observations was performed in Ambrogi et al. (2018) for the previous configuration of CTA-South: a limited worsening was obtained for sources with radial extension below 2 deg (within a factor 2 for energies above 50 GeV). Nowadays, public IRFs are available including off-axis responses, such that more detailed evaluations can be performed. In Figs. A.1, A.2, and A.3 we show respectively ASTRI, CTA-North, and CTA-South performances as a function of the offset angle R_{off} of the observation with respect to the pointing direction of the telescope (fixed to zenith of 20 deg). For ASTRI, the impact of off-axis observations will mainly consist into a reduced effective area and enlarged angular resolution. For CTA, in addition, an increase in the energy threshold is expected.

The differential sensitivities are consequently affected by off-axis observations. We performed analogous calculations to those presented in Sec. 4, this time using as input the off-axis performance. We show the results in Fig. A.4 for case off-axis observations of both point-like sources and $R_{\text{src}} = 0.5^\circ$ extended.

Appendix B: IACT sensitivity for high zenith angle observations

IACT observations at high-zenith angles are characterized by a larger effective area at high energies at the expenses of an increased energy threshold. In fact, high-energy quasi-horizontal showers can profit of a better visibility, thanks to the larger portion of the atmosphere where they develop. On the other hand, low-energy high-zenith showers are less efficiently detected as

their first interaction vertex occurs further away from the telescopes. As a result, the differential sensitivity of IACTs are affected by observations of sources at different zenith angles during the acquisition. We quantify the impact of this effect by computing the expected sensitivity for point-like observations of the CTA-N and CTA-S observatories, as shown in Fig. B.1. As visible, an improvement of a factor 2 is expected above a few tens of TeV for CTA. We expect similar considerations to hold for ASTRI as well, however we cannot proceed to a proper evaluation of it since IRFs at high-zenith angle observations are not yet publicly available.

Appendix C: Point-like differential sensitivities: comparison with official results and investigation of CTA subarrays

A cross-check of the computation methods here presented for differential sensitivities can be obtained by comparing our on-axis point-like results with the official ones released by the Collaborations (Cherenkov Telescope Array Observatory & Cherenkov Telescope Array Consortium 2021; Lombardi et al. 2022; Vercellone et al. 2022b), as in Fig. C.1. The good agreement emerging for all the observatories testifies the solidity of the methods here developed and hence its applicability to extended source studies.

For the interested reader, we further provide in Fig. C.2 the calculated point-like sensitivities of the different CTA-Alpha subarrays (SSTs, MSTs, and LSTs), as computed from the official Consortium release IRFs (Cherenkov Telescope Array Observatory & Cherenkov Telescope Array Consortium 2021), showing the role of each sub-array across the whole energy range probed by CTA.

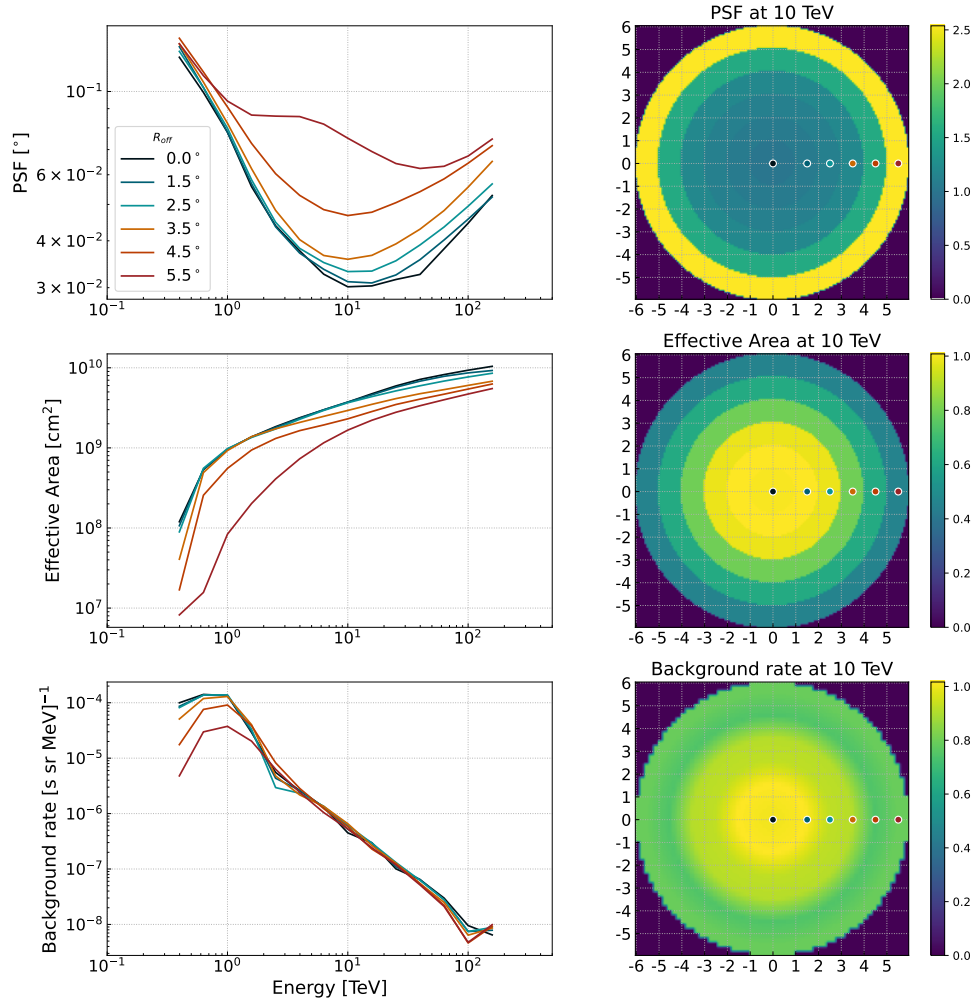


Fig. A.1. ASTRI instrument response functions (angular resolution, effective area and background rate) at different offset angles from the center of the FoV. In the left side, the IFRs are shown as a function of energy; in the right side, the degradation of the IRFs across the FoV is shown at a fixed energy of 10 TeV, where the responses are normalized to the value at the center of the field.

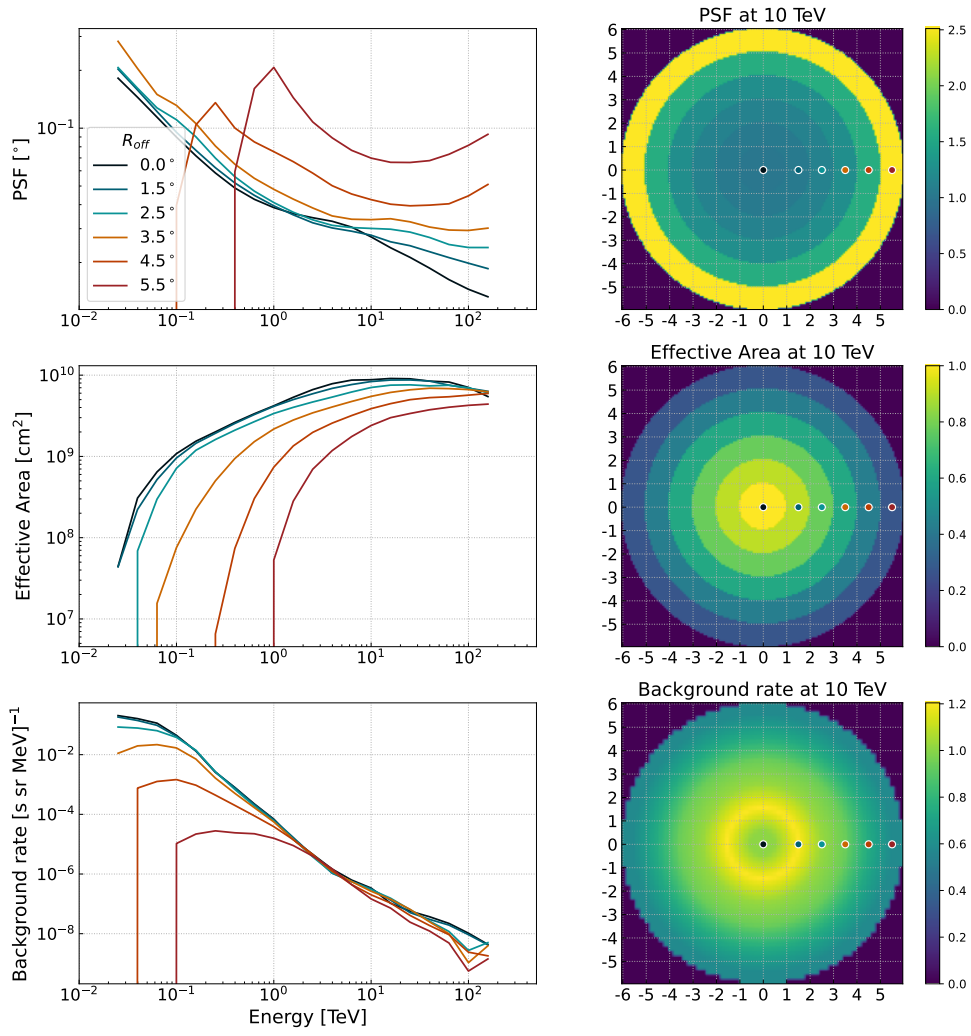


Fig. A.2. Same as in Fig. A.1, but for CTA-N IRFs.

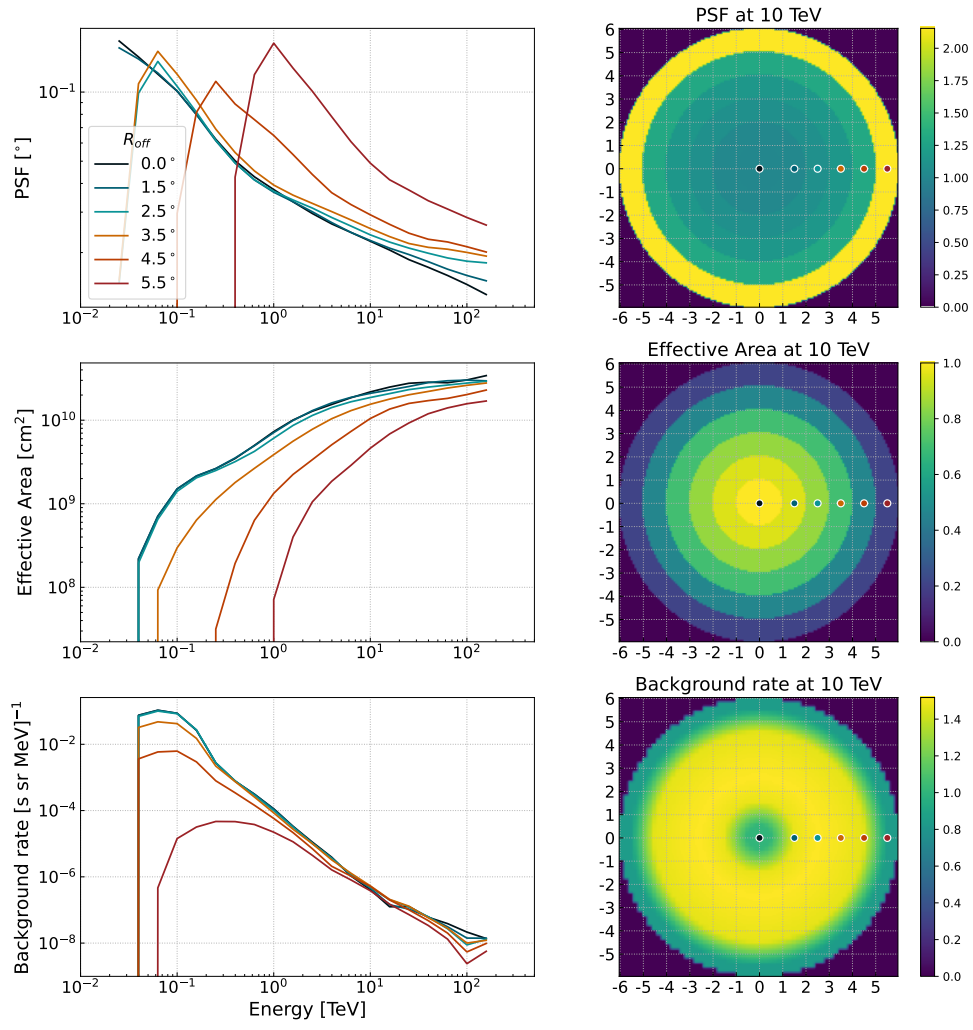


Fig. A.3. Same as in Fig. A.1, but for CTA-S IRFs.

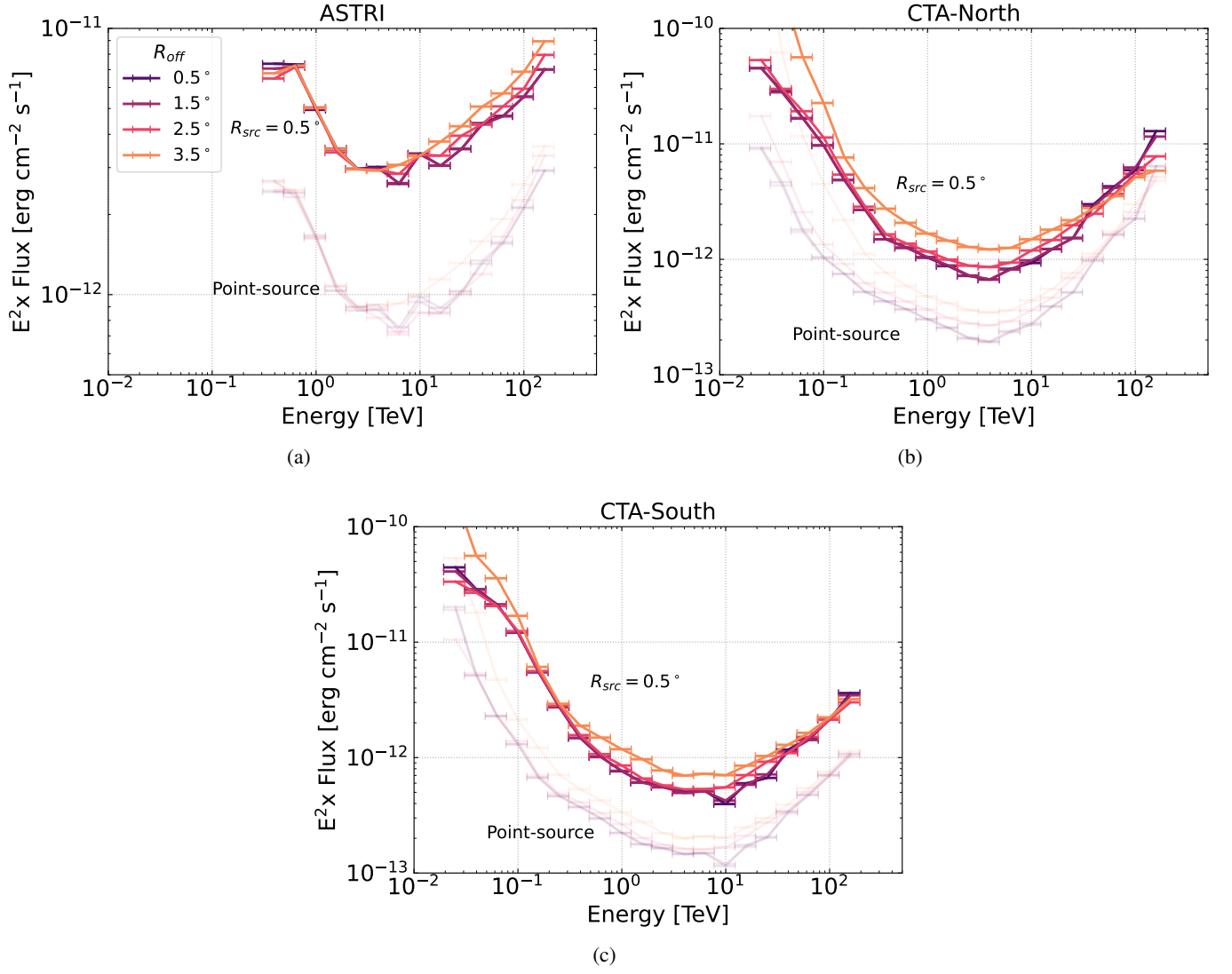


Fig. A.4. Differential sensitivities of (a) ASTRI, (b) CTA-N, and (c) CTA-S to point-like sources (shaded) and extended ($R_{\text{src}} = 0.5^\circ$, solid) displaced with respect to the telescope axis by an offset angle R_{off} , as indicated in the legend.

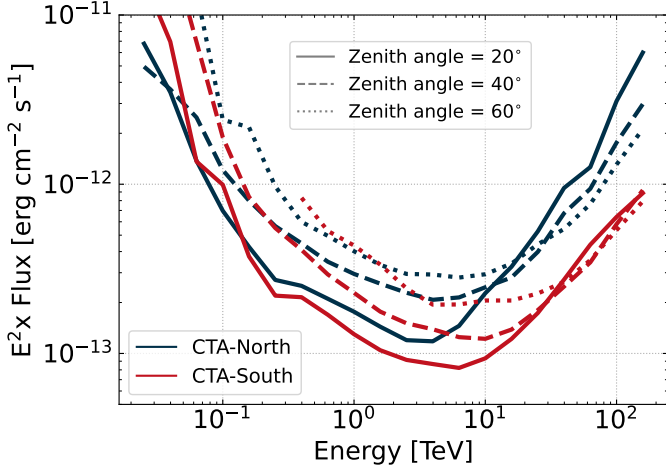


Fig. B.1. Sensitivity to point-like source observations for CTA-N and CTA-S at different zenith angles.

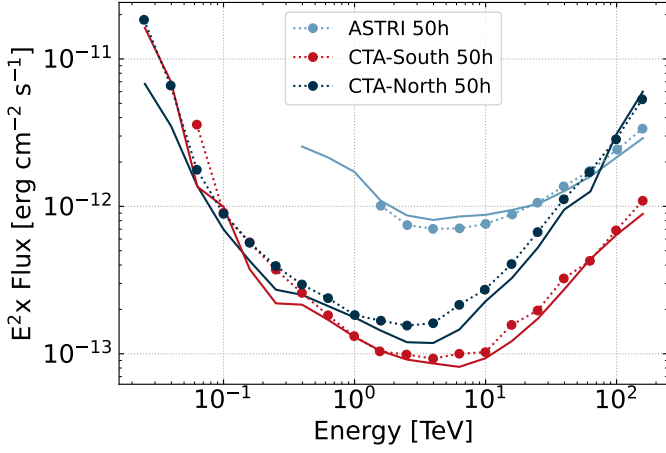


Fig. C.1. Point source sensitivity calculated in this work (solid lines) compared to the point source sensitivities released by the CTAO (Cherenkov Telescope Array Observatory & Cherenkov Telescope Array Consortium 2021) and ASTRI Collaborations (Vercellone et al. 2022b) (dotted lines). All sensitivities are calculated for an exposure 50 hours, at 20° zenith angle.

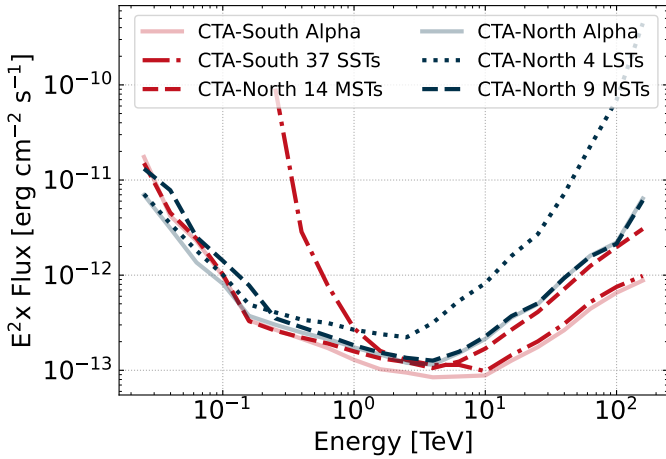


Fig. C.2. Sensitivity of the CTA-Alpha array compared to its sub-array configurations, as indicated in the figure legend.